



New insights on the fault structure of a geothermal testbed and the associated seismicity based on active seismic tomography

Miriam Larissa Schwarz¹, Hansruedi Maurer², Anne Obermann^{1,2}, Paul Antony Selvadurai¹, Alexis Shakas², Stefan Wiemer¹, and Domenico Giardini²

¹Swiss Seismological Service, ETH Zürich, Sonneggstrasse 5, CH-8092 Zürich

²Institute of Geophysics, ETH Zürich, Sonneggstrasse 5, CH-8092 Zürich

Correspondence: Miriam Larissa Schwarz (miriam.schwarz@sed.ethz.ch)

Abstract. For obtaining reliable high-resolution subsurface images in the geothermal testbed of the Bedretto Underground Laboratory for Geosciences and Geoenergies (BedrettoLab), we have applied fat ray travel time tomography. To compute a 3D velocity model, we made use of 8 boreholes, which allowed us to compile a large data set including 42'843 manually picked first breaks. We demonstrate that the fat ray approach offers improved image quality compared with traditional ray-based methods.

5 Furthermore, we have validated the 3D model using ground-truth information from wireline logs and geological observations. We succeeded in imaging a major fault zone (MFZ) that has a rather complex structure including considerable heterogeneity. Relocation of passive seismic events, generated during hydraulic stimulations, indicate that the 3D velocity model has only a minor influence on the hypocentral parameters, but a comparison of a selection of particularly well-constrained seismic events with the velocity structures revealed that there is a remarkable spatial correlation. Most events occurred in regions of 10 intermediate seismic velocities, thereby "avoiding" high and very low velocity areas. Based on small-scale laboratory studies, we speculate that these observations can be attributed to the occurrence of stress gradients in the intermediate velocity zones.

1 Introduction

Energy production from sustainable resources is a key challenge of this century. In this context, geothermal energy is recognized as a viable option. In particular, so-called “enhanced geothermal systems” (EGS) may have the potential to produce electrical energy at affordable costs (e.g. Olasolo et al. (2016); Hirschberg et al. (2015)). Key challenges include establishing sustainable flow rates, while controlling the associated induced seismicity. Examples of EGS projects that had to be stopped because of high seismicity include, for example, Basel (Edwards et al., 2015) and Pohang (Ellsworth et al., 2019). These problems are closely linked with the often poorly known fracture network of the reservoir. Therefore, several initiatives have been established to better characterize relevant host rock structures with near-field observations and well-monitored stimulation experiments. (Amann et al., 2018; Obermann et al., 2024; Kneafsey et al., 2025).

In this context, seismic measurements can offer powerful tools for imaging key structures, such as permeable fracture zones



that are the **main targets** of EGS investigations. They can be applied during an initial characterisation phase or during the stimulation phase. Generally, it can be distinguished **between** passive and active seismic techniques. Passive techniques do not
25 require actively fired seismic sources. Instead, either information contained in the ambient noise is exploited (e.g., Obermann and Hillers (2019)) or recordings from the induced seismicity are analyzed. For example, Charléty et al. (2006) conducted a 4D tomographic study using induced seismicity at the Soultz-sous-Forêts Hot Dry Rock site in France. **3D seismic velocity** structures were obtained at different times to image the temporal changes in a 4D manner.

Active seismic methods can generally be subdivided in reflection and refraction imaging and transmission tomography. Reflection and refraction imaging can be carried out either from the surface, or surface-to-borehole configurations - also referred
30 as vertical seismic profiling (VSP) techniques. In geothermal applications, VSP is particularly popular. For example, Nakata et al. (2023) used VSP data for reflection imaging of faults and fractures at the geothermal test site FORGE, Utah, U.S.A.. It is also possible to combine induced seismicity methods with reflection imaging. Block et al. (1994) applied a joint hypocenter-velocity inversion using induced seismicity from Hot dry rock (HDR) experiments at Los Alamos National Laboratory, New
35 Mexico to gain a 3D velocity model. Nakagome et al. (1998) used a seismic reflection survey together with vertical seismic profiling (VSP) to image the fractured reservoir in the Kakkonda geothermal field (Japan). Place et al. (2011) employed induced seismicity and VSP data to map fractures in Soultz-Sous-Fôrets (France). Transmission tomography primarily makes use of direct, diving or refracted waves traveling from sources to the receivers. It can be either applied from the surface (e.g., Zelt and Barton (1998); Lanz et al. (1998); Heincke et al. (2006)), or between boreholes (e.g., Pratt and Worthington (1988);
40 Maurer and Green (1997)). Here, the travel times of the first arriving waves are exploited to establish 2D or 3D distributions of the seismic velocities. Alternatively, the first break amplitudes can be used to compute attenuation models (e.g., Holliger et al. (2001)).

Since seismic waves travel in a heterogeneous medium along complicated wave paths, 2D tomographic investigations suffer from inherent limitations, resulting from the assumption that the wave paths lie exclusively within the tomographic (2D) plane.
45 Therefore, 3D investigations should be carried out, when complex subsurface structures are expected. This can be achieved quite easily with surface-based investigations, because the sources and receivers can be well distributed over the earth's surface, which results in a good seismic ray coverage of the **structures of interest**. In the case of crosshole investigations, this is often a problem, because there are rarely enough boreholes available that allow a good ray coverage of the subsurface region of interest. Therefore, 3D crosshole tomography experiments are very rare, which is unfortunate, because they can potentially
50 offer very relevant and unique subsurface information. The problem of poor ray coverage can be, at least partially, alleviated with the concept **of fat rays**. Here, it is assumed that seismic waves are not traveling along infinitesimally thin rays, but within "fat rays", whose thickness is governed by the dominant frequencies of the seismic waves. Initial concepts were provided by Woodward (1992) , and fat ray approaches were implemented for local earthquake tomography (Husen and Kissling, 2001) and active seismic experiments (Jordi et al., 2016).
55 In the framework of the host rock characterization of the Bedretto Lab (Ma et al., 2022; Plenkers et al., 2022), an **unusually** large number of boreholes were drilled within a geothermal testbed at **hectometer scale**. Such a setup is particularly useful for 3D travel time tomography, making it possible to illuminate the entire volume of interest. Consequently, various active seismic



crosshole measurements were carried out. In addition to the good borehole coverage, we benefited from the advantageous features of fat ray tomography, and we could establish a well-constrained 3D velocity model that is valuable for characterizing 60 critical host rock structures.

We start with a short description of the Bedretto Lab and the embedded geothermal testbed. Then, we present our data set, followed by a short description of the methodology employed to establish the 3D velocity models. After the presentation of the tomographic results, we perform a joint interpretation with geological and geophysical add-on data sets that were also acquired at our test site. In particular, we discuss the spatial correlation between passive seismic events and the velocity structures found.

65 2 Site description

The Bedretto Underground Laboratory for Geosciences and Geoenergies (BULGG or BedrettoLab), operated by ETH Zurich, is located in the central Swiss Alps (Ticino) in a 5.2 kilometres long side tunnel of the Furka railway tunnel (Figure 1a). The BedrettoLab is a unique research facility that provides optimal conditions for conducting experimental research on understanding the responses of the deep underground during hydraulic stimulations. With dimensions at the hectometer scale, 70 the BedrettoLab closes the gap between the decameter laboratory scale (e.g. Grimsel test site (Gischig et al., 2020) and the reservoir scale (Amann et al., 2018).

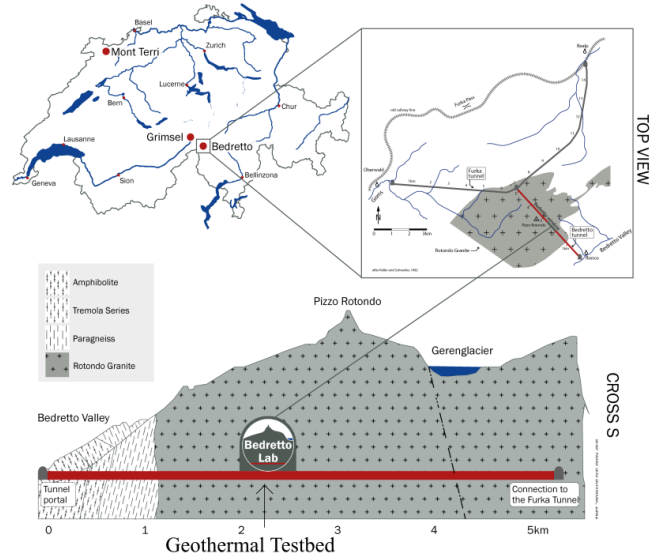
The BedrettoLab host rock is called the Rotondo Granite. Its intrusion into the Gotthard Massif took place during the late Variscan orogeny (Sergeev et al. (1995)). In general, the Rotondo Granite is relatively homogeneous with only slight influences of metamorphism (Labhart T, 2005; Lützenkirchen and Loew, 2011). The general maximum horizontal stress direction 75 lies within the NW quadrant (Heidbach et al., 2018). Bröker and Ma (2022) discussed the effect of variations in the topography along the tunnel that can cause fluctuations of the local stress field. A previous study of Meier (2017) revealed that the topographic effect decreases with increasing overburden and can be neglected after tunnel meter 1500 m, where it is assumed to be vertical. There are some indications of a slight anisotropy of the host rock, which is expected to also affect the seismic velocities (Behnen et al., 2024), but for the sake of simplicity, we assume an isotropic velocity model.

80 The geothermal testbed is located between tunnel meters 2000 m to 2100 m, measured from the tunnel portal (see Figure 1a)). It has an overburden of about 1030 m. It includes several boreholes, ranging from 250 m to 400 m length. The six monitoring boreholes (MB1, MB3-MB5, MB8) are equipped with a state-of-the-art monitoring system. This includes seismic sensors (geophones, accelerometers and acoustic emission) as well as active seismic sources (piezoelectric transducers). In addition, a stimulation (ST1) and an extraction (ST2) borehole were drilled into the testbed. ST1 was equipped with a multi-packer 85 system, with which it was subdivided into 14 intervals (Bröker et al., 2024), and ST2 was kept open for the use of various measurements, for example, active seismic measurements with the P-wave sparker. For more details on the multi-disciplinary monitoring system, we refer to the overview paper of Plenkers et al. (2022).

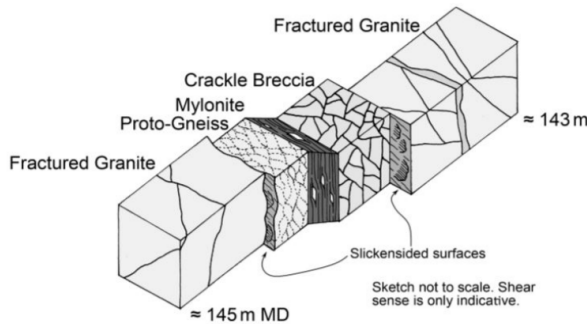
Faults and fractures within the geothermal testbed have been mapped mainly as subvertically dipping, predominantly striking 90 NE-SW to ENE-WSW (Labhart T, 2005; Lützenkirchen and Loew, 2011) and frequently steeply dipping, striking N-S and E-W along the tunnel (Jordan, 2019). Ma et al. (2022) and Bröker et al. (2024) show detailed maps of fractures along the



(a) Geological map + BedrettoLab



(b) Schematics of the fault zone structure in MB1



(c) Boreholes in main axis system and fault zone

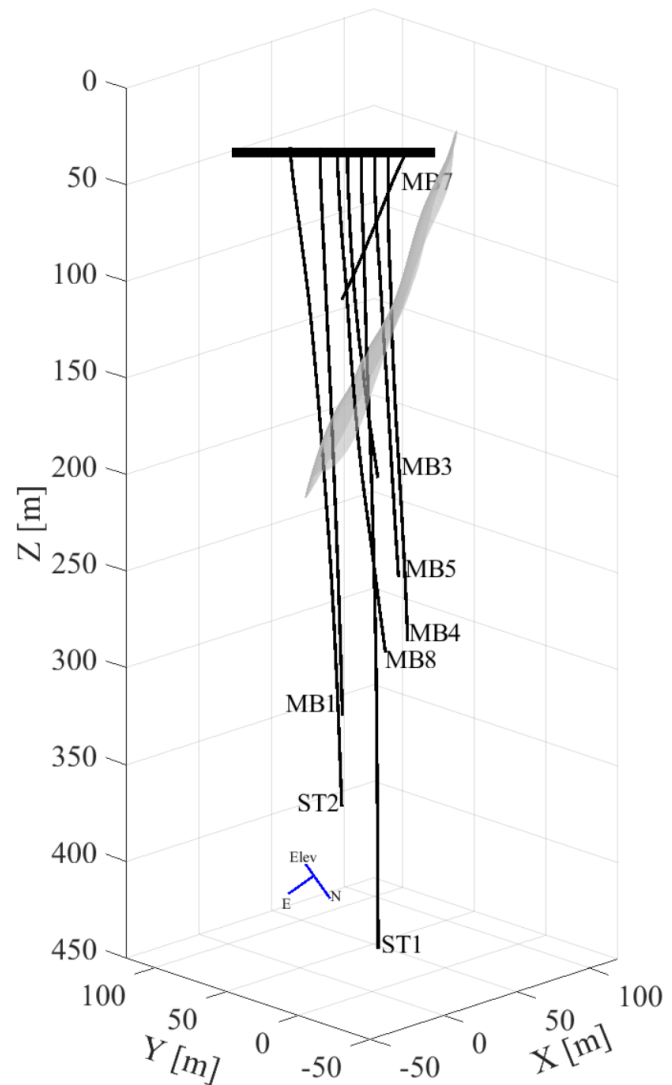


Figure 1. (a) Location and geological map of the BedrettoLab. (b) Schematics of the fault zone measured from MB1. The fault zone is between 143 and 145 m depth in this borehole. Fractured Granites surround Porto-Gneis, Mylonite and Crackle Beccia. Figure adjusted from Ma et al. (2022). (c) The Geothermal Testbed contains six monitoring boreholes (MB1, MB3-MB5, MB7, MB8) and one stimulation (ST1) and one extraction (ST2) borehole with lengths between 100 and 400 m. The boreholes are rotated into the tomography coordinate system. The advantages of the rotation are a smaller amount of model parameters and positive axes for the inversion. The blue arrows show the orientation of the original Bedretto coordinate system with Easting, Northing and Elevation, which is used in many other BedrettoLab-related publications. The main fault zone in this area is shown as gray surface and is referred to as "Major Fault Zone" (MFZ) within this paper (fault zone after Escallon et al. (2024)). For the following analysis this representation is used.



tunnel, which are based on tunnel wall mapping and borehole logging. The fractures can be divided into four different sets: striking N–S, NE–SW/tunnel perpendicular, E–W, and NW–SE/tunnel parallel.

A major fault zone (MFZ) within the geothermal testbed is of particular interest for this study. It was discovered by previous studies using all boreholes available. Escallon et al. (2024) imaged the MFZ using GPR reflection measurements, and this was 95 validated by borehole televiewer observations (ATV / OTV) that have been described by Ma et al. (2022). The MFZ is shown as a gray surface in Figure 1c). Ma et al. (2022) gives a schematic of the fault zone structure based on borehole cores (Figure 1d): the fault zone in MB1 ranges from 143 m–145 m MD (measured depth). Fractured Granite surrounds Proto-Gneis, Mylonite and Crackle Breccia.

3 Data

100 Within the scope of the characterization of the geothermal testbed, a large variety of geophysical and geological measurements were carried out. This included active seismic crosshole measurements. The full data set contains several independent surveys that were taken at different times from October 2020 to November 2021, depending on when the boreholes were drilled and being available. A detailed overview is given in Table 1. The borehole configuration is shown in Figures 1b and 1c. The spacing of the source varied between 1 m, 2 m, and 5 m for the different surveys and along the borehole depths.

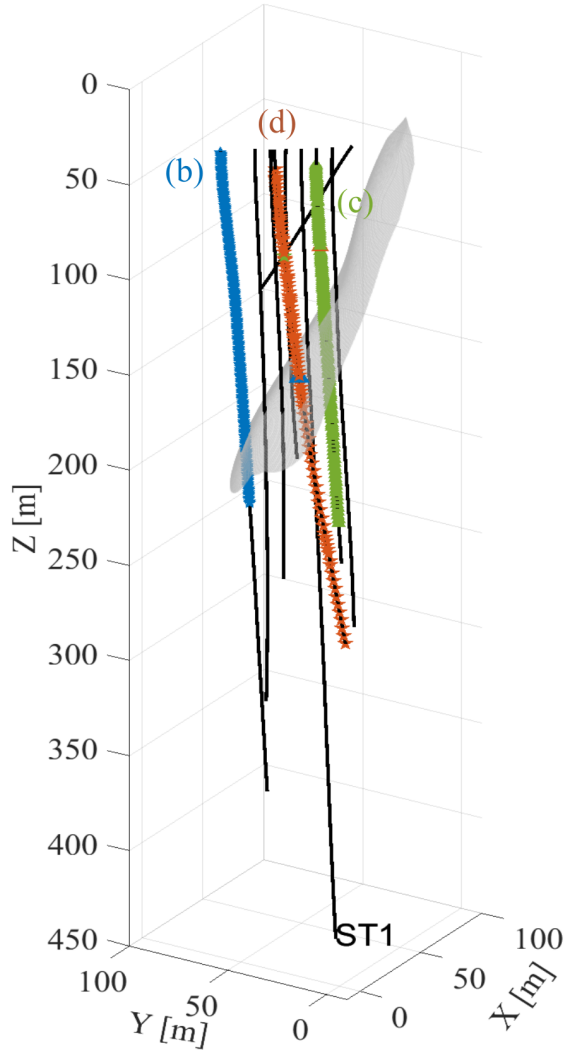
105 As a source we employed a seismic P-wave sparker with a dominant frequency band of about 1 to 10 kHz (<https://geotomographie.de>). The first three data sets were recorded on two hydrophone chains with 1 m and 2 m spacing, respectively (Table 1). The surveys were designed such that the receiver/shot spacing is denser around the MFZ and sparser at larger distances away from it. These surveys were conducted before the instrumentation and cementation of the boreholes. The last survey was carried out in November 2021, after the instrumentation, but prior to stimulation experiments. Permanently installed acoustic emission 110 (AE) sensors were used as receivers, and they had to be synchronized with the sparker setup. For each source point and all surveys, the sparker source was fired three times, and the traces were then stacked to enhance the signal-to-noise (SNR) ratio. Overall, we were able to compile a relatively large data set including 42'843 manual P-picks (Table 1) with a average picking uncertainty of about 0.15 ms. Source-receiver distances varied between 10 m and 186.5 m.

115 In Figure 2 we show three examples of shot and receiver gathers. Figure 2a) shows the setting with the source and receiver configurations as well as the MFZ. 2b) displays a receiver gather recorded on the AE sensors (sensor in MB8, sources in ST2), 2c) shows a receiver gather recorded on a hydrophone (sensor in MB5 and receiver in MB8) and 2d) shows a source gather recorded on hydrophones (source position in MB5 and receivers in MB8). The first arrivals of the P-waves, indicated by the yellow arrows, are clearly visible. The P-wave sparker, as the name suggests, is designed to generate primarily seismic P-waves. S-waves that are visible in the data are therefore most likely converted P-to-S phases, with the conversion likely taking place 120 at the source borehole wall. The S-waves are shown in Figures 2b, c, and d, (indicated with purple arrows). They are generally difficult to pick, because they often overlap with scattered parts of the P-waves or with reflected waves. Therefore, we restrict ourselves to the first arriving P waves.

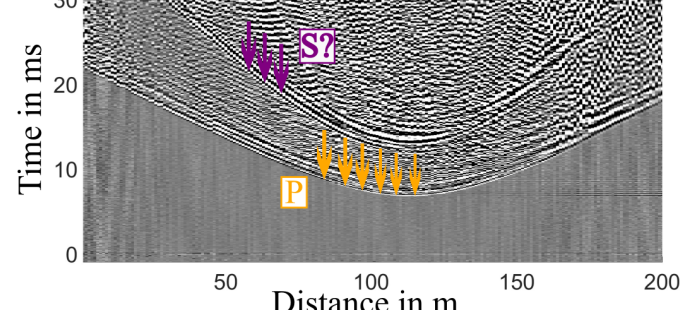
Figure 3 shows example traces from a hydrophone and an AE sensor with a similar source-receiver distance. Furthermore,



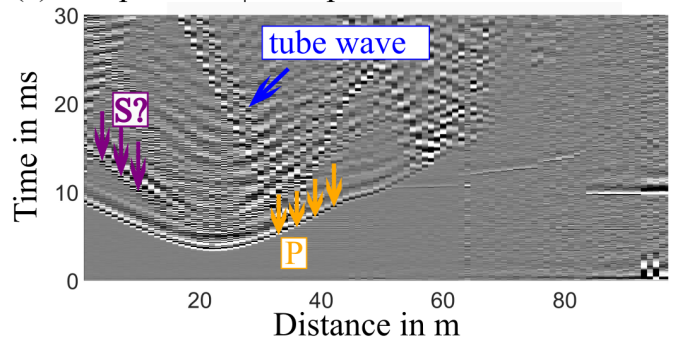
(a) shot and receiver positions



(b) Rec pos: 228 | Shot pos: 1 to 200



(c) Rec pos: 113 | Shot position 1 to 180



(d) Shot pos: 38 | Rec pos: 70 to 355

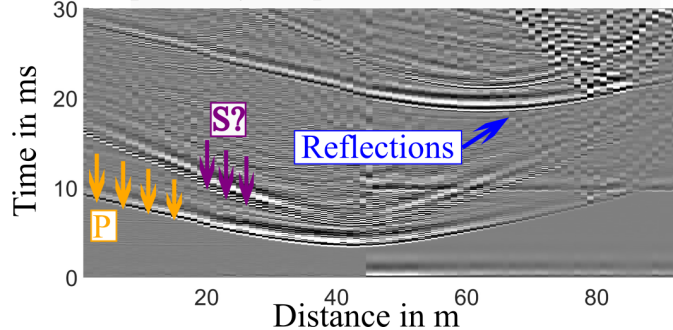


Figure 2. Shot and receiver gather. Figure a) shows the shot (stars) and receiver (triangles) positions for the waveforms shown in b), c) and d). The grey surface indicates the MFZ. b) displays the receiver gather recorded on the AE sensors, c) shows a receiver gather recorded on a hydrophone and d) shows a source gather recorded on a hydrophone. First arrivals for P-wave are indicated with yellow arrows, and examples for reflections are indicated with blue arrows. Red arrows denote systematic noise patterns of unknown origin. The predicted S-wave arrivals are indicated with purple arrows.

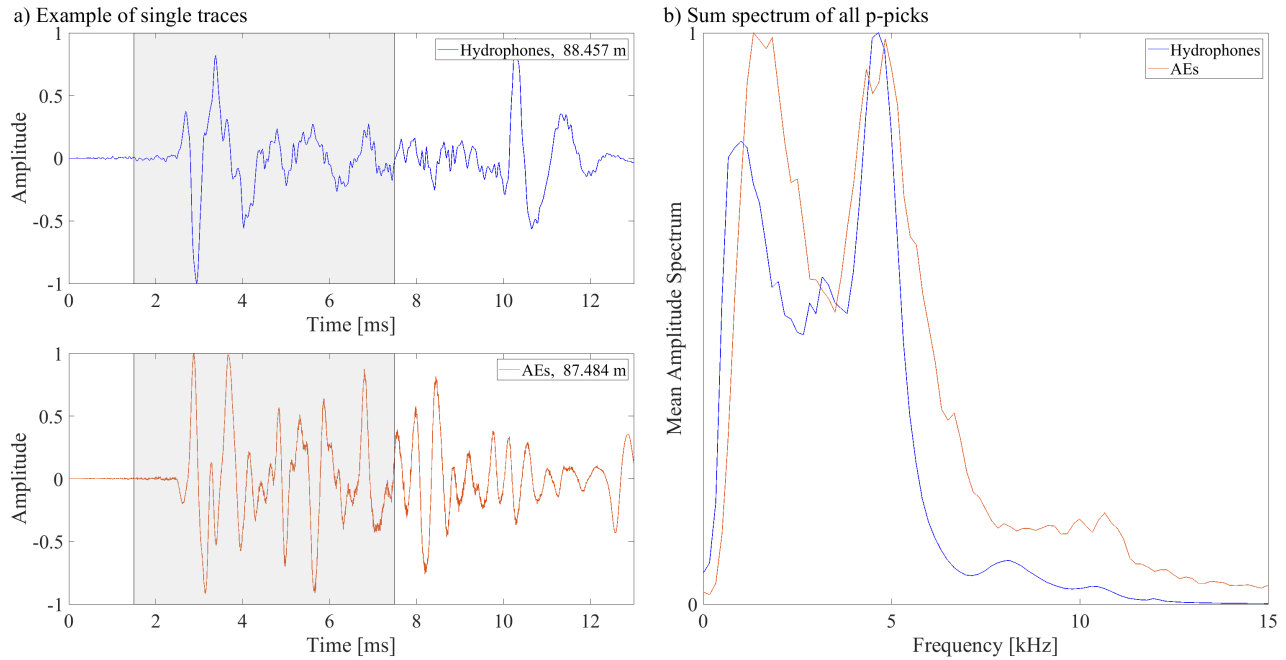


Figure 3. a) **Example of the data.** Top: single trace of the hydrophone data. Bottom: single trace recorded on an Acoustic Emission sensor (AE), both show a **nicer** signal-to-noise ratio. Both signals are recorded at a similar source-receiver distance. The grey box indicates the time window that is used to calculate the **sum spectra**. For visualisation purposes we normalized the data to the maximum amplitude. b) shows the sum spectrum of all p-picks, which reveals a frequency band between 1 kHz and 7.5 kHz. We normalized the sum spectrum for a better comparison.

the summed amplitude spectrum of the P-wave for **all** hydrophone and AE sensor recordings, where a first break onset could
125 be picked, is shown. A time window of 6 ms around the first break was taken to calculate the amplitude spectra, which were then summed to obtain the sum spectrum. The frequency content of both sensor types is comparable, with the energy of the first-arriving waves varying between 1 kHz and 7.5 kHz. It should be noted that the sharp decrease below 1 kHz is caused by analog filters of the acquisition systems. Furthermore, it is noteworthy that there is a significant decrease of spectral amplitudes around 3 kHz for both sensor types. Since the hydrophone and AE data were acquired with different acquisition systems and
130 the sensor types are quite different, **this is likely caused by the attenuation properties of the host rock.**

4 Travel time tomography

Seismic travel time tomography is a **well-established procedure** (e.g., Nolet (1987)). It requires (i) an initial model, (ii) a forward solver to predict the travel times for a given model, (iii) an inverse solver to estimate the seismic velocities (resp. the seismic slownesses, the inverse of velocity) from the observed data, and (iv) a regularization scheme to account for the



Table 1. Acquisition parameters of the seismic survey

borehole source	borehole receiver	shot spacing	receiver spacing	sensor	date	number of traces	number of picks
ST1	ST2	2 m	1m/2m	hydrophones	Oct. 2020	15307	7413
MB4	MB1	2 m	1 m	hydrophones	Oct. 2020	5376	3716
MB3	MB4	2 m	1 m	hydrophones	Oct. 2020	3648	1780
MB3	MB1	2 m	1 m	hydrophones	Oct. 2020	1824	1337
MB1	MB4	2 m	1 m	hydrophones	Oct. 2020	2976	1620
MB8	MB7	5 m/2 m	1 m/2 m	hydrophones	June 2021	4840	2476
MB8	MB5	5 m/2 m	1 m/2 m	hydrophones	June 2021	13698	7143
MB5	MB7	5 m/2 m	1 m/2 m	hydrophones	June 2021	6644	4610
MB5	MB8	5 m/2 m	1 m/2 m	hydrophones	June 2021	14562	9437
ST2	MB1	1 m	fixed depth	AE sensors	Nov. 2021	800	179
ST2	MB3	1 m	fixed depth	AE sensors	Nov. 2021	1400	781
ST2	MB4	1 m	fixed depth	AE sensors	Nov. 2021	1200	667
ST2	MB4	1 m	fixed depth	AE sensors	Nov. 2021	1200	667
ST2	MB5	1 m	fixed depth	AE sensors	Nov. 2021	800	539
ST2	MB7	1 m	fixed depth	AE sensors	Nov. 2021	200	158
ST2	MB8	1 m	fixed depth	AE sensors	Nov. 2021	1600	987
total number of traces:	74875						
total number of picks:	42843 (57.2%)						
source type:	P-wave sparker						
sampling frequency							
hydrophones:	48 kHz						
AE sensors:	200 kHz						

135 underdetermined components of the inverse problem (e.g. Menke (1984)). As a forward solver we considered the algorithm by Podvin and Lecomte (1991), which solves the Eikonal equation on a regular grid with a finite-difference approach. The seismic rays are then computed with a backtracing algorithm (Li et al., 2018). To solve the inverse problem, the volume of interest needs to be discretized in 3D cells of an adequate size. Note that the discretization used for the forward solver and for the inverse problem do not need to be identical. Then, the ray segment lengths for each inversion cell and source-receiver
140 pair are determined and fed into the $n \times m$ Jacobian matrix \mathbf{J} , where n is the number of data points and m is the number of inversion cells. Since such tomographic problems always include an underdetermined component, regularization of the inverse problem is required. For that purpose, we have added damping and smoothing constraints (see Maurer et al. (1998) and Lanz



et al. (1998) for further details). The inverse problem can then be written as

$$\begin{pmatrix} \mathbf{J} \\ \mathbf{D} \end{pmatrix} \mathbf{s} = \begin{pmatrix} \mathbf{t} \\ \mathbf{h} \end{pmatrix}, \quad (1)$$

145 where \mathbf{J} is the Jacobian matrix, \mathbf{t} the observed travel times, \mathbf{D} and \mathbf{h} the regularization constraints, and \mathbf{s} the unknown slow-
nesses. The resulting system of equations in 1 is typically very sparse and can thus be solved conveniently with the LSQR
algorithm proposed by Paige and Saunders (1982). With the updated velocity model, the predicted travel times and the ray
geometry need to be recomputed to update \mathbf{J} . This procedure is then repeated until convergence is achieved.

150 Since infinitely thin rays, computed with the Eikonal equation, are not a good physical representation of finite-frequency seis-
mic waves, and they often cover not all inversion cells, the concept of fat rays was introduced by Woodward (1992). The
underlying idea of this concept is to extend the thin rays to a width that corresponds to the dominant wavelengths of the data
observed. When the travel time fields from the solution of the finite-difference Eikonal solver are available, the region of the
fat rays can be calculated swiftly with the formula of Červený and Soares (1992) that describe the first Fresnel volume, which
is equivalent to the fat ray

155 $|t_{sx} + t_{rx} - t_{sr}| \leq T.$ (2)

t_{sx} and t_{rx} are source or receiver travel times to an arbitrary point x within the forward modeling domain, t_{sr} is the predicted
travel time with the actual model \mathbf{s} and T is the dominant period of the seismic waves. When the inequality in Equation 2 is
satisfied, the point x lies within the fat ray volume. To compute the fat ray volumes, it is necessary to not only solve the forward
problem for each source position, but also for each receiver position, which can increase the computational costs significantly.

160 For computing the fat ray Jacobian matrix, it is necessary to compute for every source-receiver pair a function f_x , defined as

$$f_x = \begin{cases} T - t_{sx} - t_{rx} + t_{sr}, & \text{if } |t_{sx} + t_{rx} - t_{sr}| \leq T \\ 0, & \text{otherwise} \end{cases} \quad (3)$$

at every grid point of the forward model. Then, the f_x values, contained in a particular inversion grid cell, are summed up
and inserted into the corresponding element of \mathbf{J} . Finally, each row of \mathbf{J} needs to be scaled, such that $\mathbf{J}\mathbf{s} = \mathbf{t}_{sr}$ is enforced.

165 Husen and Kissling (2001) and Jordi et al. (2016) implemented similar concepts of fat rays for local earthquake tomography
and controlled-source tomography respectively.

5 Application to field data set

5.1 Setup of the inversion

For the travel time tomography we used the data presented in Section 3. A homogeneous velocity model of 5300 m/s was used
170 as starting model, estimated from travel time curves of our data. The coordinate system was rotated into the main axis system

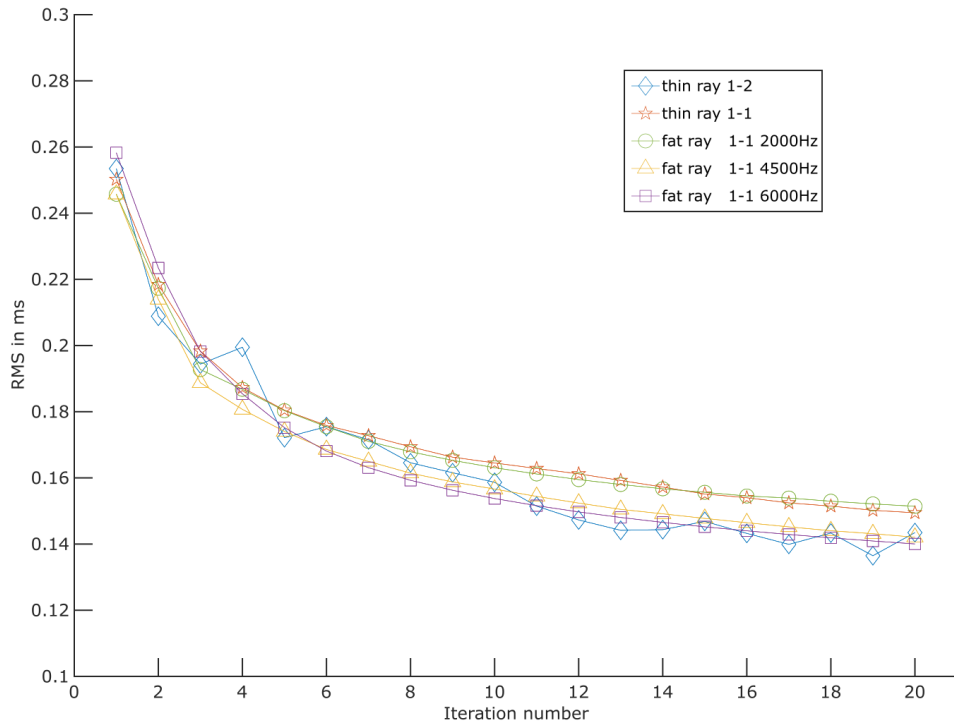


Figure 4. Development of the RMS discrepancy between observed and predicted travel times for different configurations: the thin ray based tomography with two different cell sizes of the inverse solver (**1 m** and **2 m**) and the fat ray tomography with different frequencies, 2 kHz, 4.5 kHz and 6 kHz. Fat ray inversions employed the same grid for the forward solution and inversion $1 \times 1 \times 1 \text{ m}^3$. The same applies to the thin ray 1-1 inversion. For the thin ray 1-2 inversion, 8 forward cells were merged to larger cubic inversion cells.

(or principle axis system) of the borehole trajectories to reduce the number of numerical cells. This resulted in a model of dimension of $72 \times 62 \times 406 \text{ m}^3$. We compared different cell sizes for the thin ray-based approach, referred to as "thin ray". The inversion cell size was either 2 m or 1 m, but the forward solver cell size was always kept at 1 m.

The convergence behavior of the different inversion runs is shown in Figure 4 in the form of **RMS curves**. For the fat ray tomography, we always used the smaller inversion cell size of 1 m and compared different frequencies: 2 kHz, 4.5 kHz and 6 kHz that are within the frequency spectra of the P-wave (see Figure 3). With appropriate regularization for the different inversions, all inversion runs converged reasonably well, that is, the RMS curves are flattening out, and they all show a similar convergence behavior. However, for the thin ray inversion with 1 m cell size and for the fat ray inversion with 4.5 kHz and 6 kHz, **more regularization** was required to account for the larger underdetermined component of the inversion problem. Generally, the RMS reduced from 0.25 ms to approximately 0.15 ms within 20 iterations, which is consistent with our picking accuracy. Since we did not observe significant differences in the convergence behavior of the different settings, and the resulting tomography



models were similar, we have chosen 2 kHz for our fat ray tomography to obtain the best spatial coverage with the lowest reasonable frequency. An overview of the different slices through the models that we show in this paper, including the MFZ, is shown in Figure 5.

185

5.2 Comparison of Thin ray and Fat ray tomography

To show the benefit of the fat ray approach, we compare the 2 kHz fat ray results with the thin ray results. For the comparison, we consider the column sums of the Jacobian matrix, subsequently referred to as "coverage", as, for example, described in Jordi et al. (2016). The summation of the j th column of the Jacobian matrix gives an estimate of the overall sensitivity related 190 to the j th inversion cell.

In Figure 6, we compare the velocity tomograms for the thin ray (6a) and the 2 kHz fat ray (6b) at 150 m depth. Higher velocities are displayed in blue, lower velocities in red, and the mean velocity ($\approx 5340 \text{ m/s}$) is represented in gray. Areas with insufficient coverage are shown in white. The green line indicates the MFZ at this depth. Figure 5 shows an overview of the 195 slice with the boreholes and the MFZ. Both tomograms show similar features, but the structures in the fat ray tomogram (Figure 6b) are much clearer. Considering the fact that the fat rays are a better physical representation of the actual finite frequency wavepaths, one can conclude that the tomogram in Figure 6b is not only clearer, but also likely more reliable, and the thin ray 200 tomogram in Figure 6a, which additionally suffers from coverage problems. In the following, we restrict our discussion to the fat ray tomographic model that was computed with a frequency of 2 kHz.

200 5.3 3D velocity model

P-wave velocities in the tomographic model vary between 4685 m/s and 6212 m/s, and the mean velocity is at about 5340 m/s. Figure 7 displays horizontal slices through the final velocity model at different depths. Figure 7 shows the tomographic 205 velocities in (a) and the corresponding coverage in (b) at different depths. An overview of the different slices together with the boreholes and the MFZ is given in Figure 5. The intersections with the boreholes are shown as black dots (a) and blue dots (b), respectively. The intersection of the slice with the MFZ is shown as green line. There is a conspicuous low-velocity feature at $z = 150 \text{ m}$, which is similar to the feature visible in Figure 6a. Its signature is also weakly visible in the horizontal slice at $z = 100 \text{ m}$, but is absent at $z = 200 \text{ m}$. The highest velocities are observed in the slice at $z = 100 \text{ m}$.

A vertical slice through the model is provided in Figure 8. Since the MFZ (see Figure 1) is a feature of major interest, we provide a vertical section perpendicular to the strike of this fault zone through the central part of the 3D model. The vertical 210 section confirms that there are predominantly low velocities between $z = 100 \text{ m}$ to $z = 150 \text{ m}$, and uniformly higher velocities are observed at greater depths. Below $z = 250 \text{ m}$, the coverage and thus the reliability of the velocity model is very low.

The horizontal and vertical slices in Figures 6 and 8 provide some insights into the structure of the 3D velocity model. However, such single slices can be difficult to interpret. Therefore, we have created a series of videos, with which it is possible to

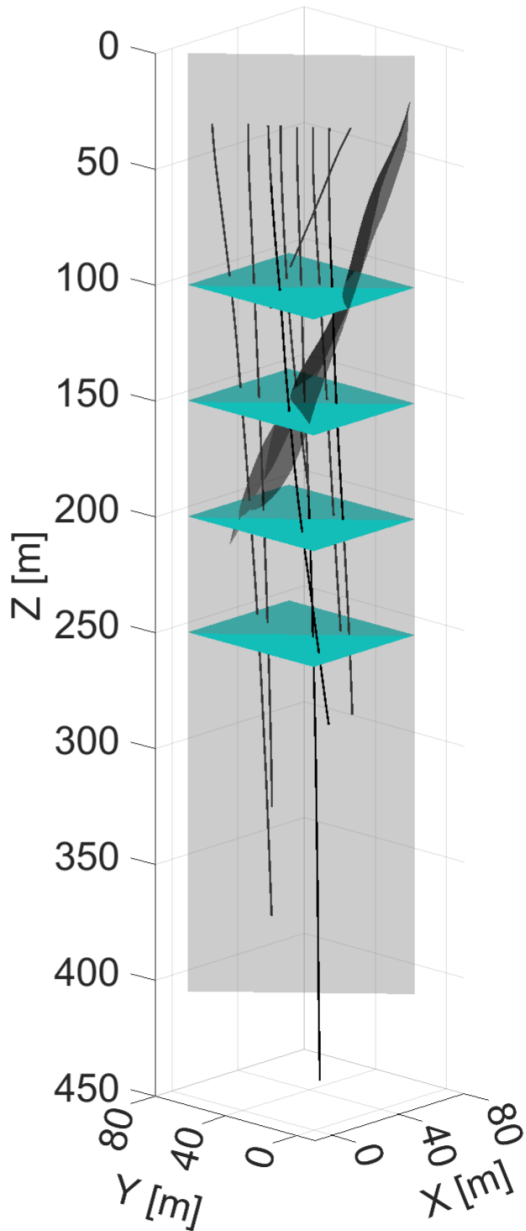


Figure 5. Overview of the different slices that are shown in Figure 6 (slice at 150 m), Figure 7 (slices at 100 m, 150 m, 200 m and 250 m) and Figure 8 (slice perpendicular to the MFZ).

scan in various directions through the model cube. They are provided in the digital appendix, and it is highly recommended to
215 make use of them to better understand the structures contained in the 3D model.

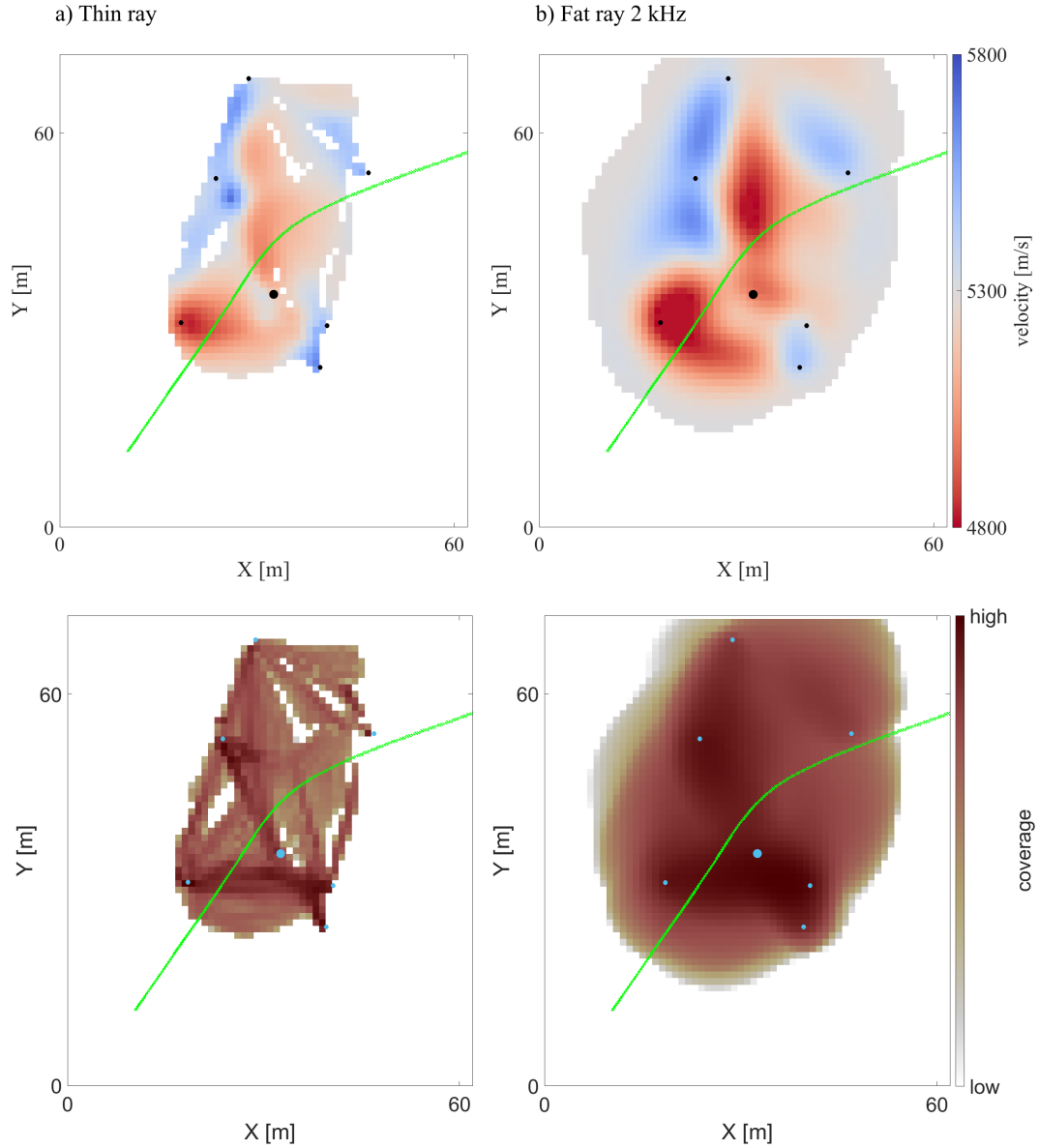


Figure 6. Tomograms of the **final velocity model** in x-y-plane at $z = 150\text{ m}$: (a) tomogram of the thin ray approach, (b) tomogram of the 2 kHz fat ray approach. Unresolved areas are left white. The dots indicate the intersections of the boreholes with the slice at $z = 150\text{ m}$, while the larger dot indicates the borehole ST1. The upper tomograms show the velocities, the lower one show the corresponding **coverage** of the model. The green line shows the intersection of the MFZ with the x-y-plane at 150 m .

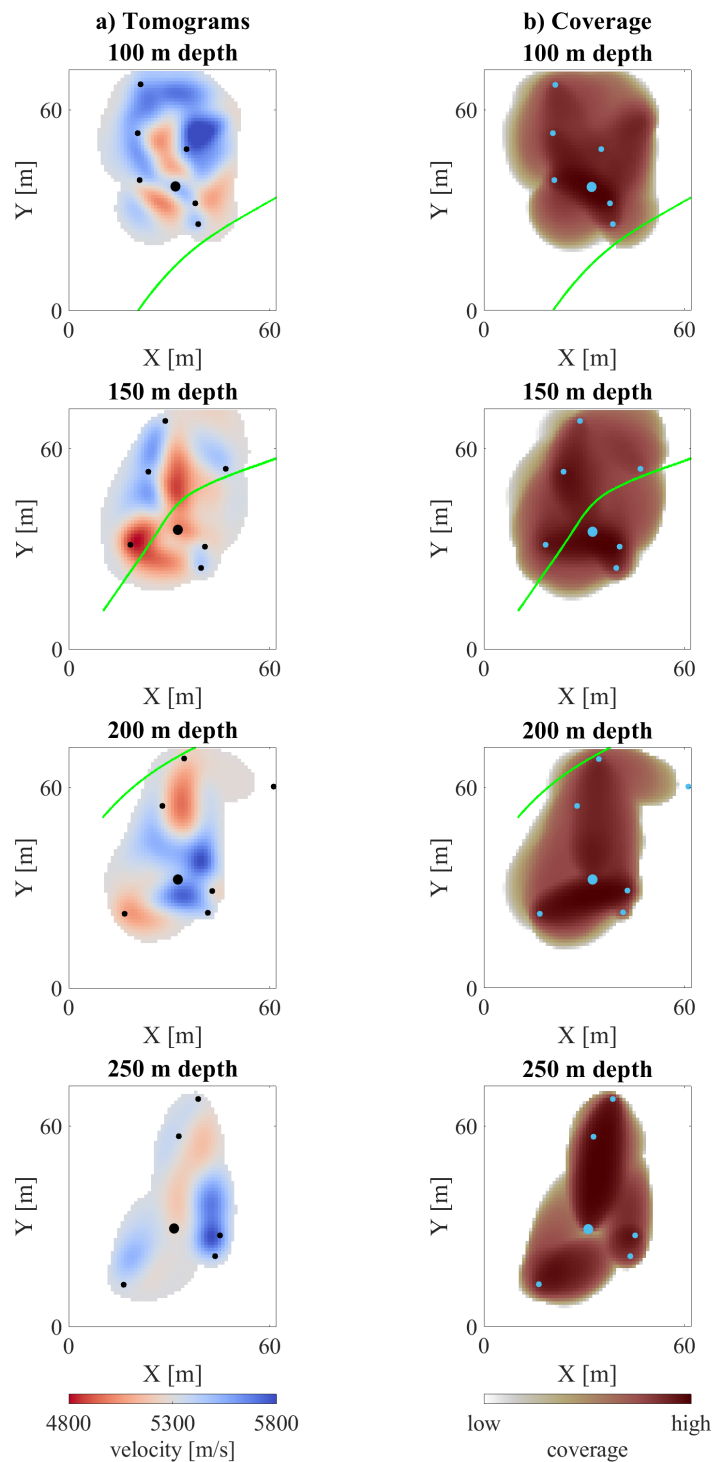
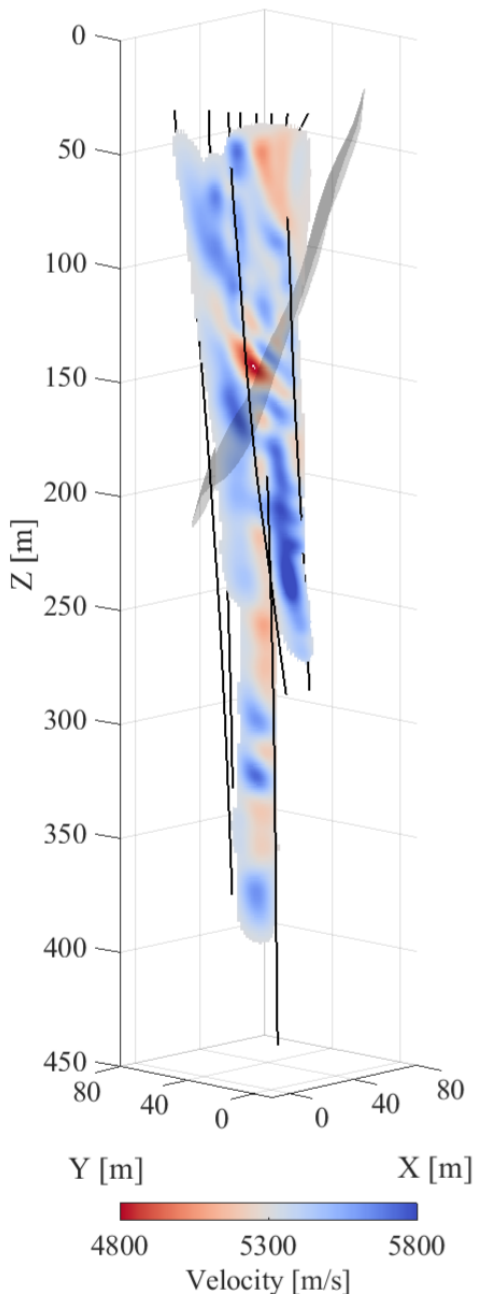


Figure 7. a) Velocity tomograms at different depths and the corresponding coverage in b). Unresolved areas are left white. The dots indicate the intersections of the boreholes with the slice, the larger dot indicates the borehole ST1. The green line indicates the intersection with the MFZ.



a) Tomogram



b) Coverage

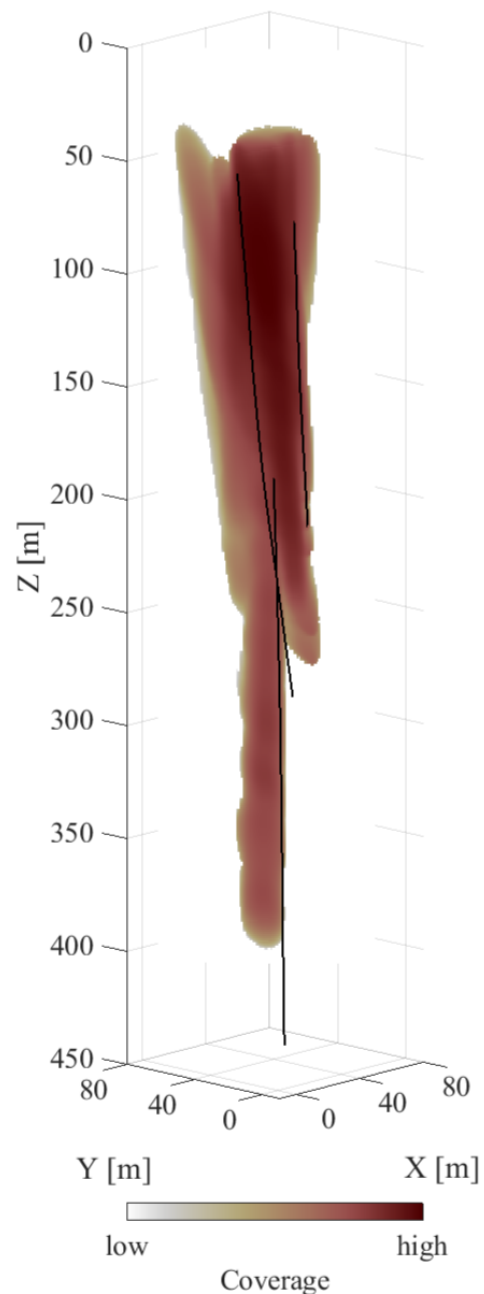


Figure 8. a) shows a tomogram perpendicular to the fault zone as gray surface (data from GPR measurements (Escallon et al., 2024)). b) shows the same slice but for the coverage of the model. It shows, that the **coverage** is good between 50 m to 230 m but **with a linear shape**. The linearity of the **low-velocity zone** with the depth direction might be caused by lower coverage at the edges of the model.



5.4 Validation of the velocity model with independent data sets

Laboratory measurements at fluid-saturated undisturbed core samples indicated values up to $V_p=5434$ m/s. From these results, P-wave velocities at in-situ conditions with $P_{eff}=15$ MPa were estimated to be 6123 m/s (David et al., 2020). This is broadly consistent with the maximum values observed in the tomograms (6212 m/s).

220 Another option to validate the velocities obtained by the tomographic inversions is offered by sonic logs, acquired in borehole ST1. A comparison is shown in Figure 9. To compare both datasets, the sonic logs were downsampled to the sampling rate of the tomographic velocity model. The tomographic velocities are shown in black, those from sonic logs in orange. Adjacent to the velocity profiles, we have also extracted the **coverage** values along ST1, shown as blue line. They show that the depth range of trustworthy tomographic velocities lies between 50 m and 230 m (denoted by horizontal dashed lines in Figure 9. As 225 a consequence, the tomographic velocities above and below the depth range resolved are close to the initial velocities of 5300 m/s.

In the depth range resolved, the sonic logs show slightly higher velocities compared with the tomographic results. This is expected because the sonic logs employ higher frequencies. Therefore, the comparison with the sonic logs is rather restricted to relative velocity changes. Both curves show a significant low-velocity anomaly at about 150 m depth. To verify this low- 230 velocity zone as a feature of the MFZ, we compare it with ATV measurements (Figure 9, right panel) at this depth. We show the **ATV travel time**, adapted from Bröker et al. (2024). The ATV measurements reveal a broad fracture zone shown by an increase in ATV travel time up to $180 \mu s$. A more detailed analysis of the borehole cores is shown in Bröker et al. (2024) e.g. 235 Figure 3). They compare different borehole logs from ST1 and concluded that temperature, conductivity, spinner up and ATV logs all show a prominent structure in Unit 3 indicated as "Largest fracture zone". The different geological measurements show a variety of smaller breakouts and fractures. However, it seems that the tomographic velocities are mostly sensitive to the MFZ. 240 The comparisons of the 3D seismic model with the borehole logs and borehole cores shows a generally good agreement along ST1. So the question arises, if the **tomographically derived velocity structures** allow delineations and characterizations further away from the boreholes, where no ground truth information is available. For that purpose, we compare the **tomographically derived velocities** with the geometry of the MFZ, as derived by Escallón et al. (2024). In Figures 7 and 8, the MFZ structure is 245 **superimposed**. If the MFZ would be a clearly confined zone, one would expect a correspondingly well-confined low-velocity zone in the velocity model. Instead, we observe generally decreased velocities along the MFZ traces, but there is also a substantial amount of heterogeneity. This may be partially the result of the limited spatial resolution power of the tomograms, but it most likely indicates that the MFZ is a complex faulting structure, affecting larger volumes of the host rock, and including substantial heterogeneities.

245 5.5 Appraisal of rock quality

The velocity variations found in the tomographic volume are relatively small, and 99% of the velocities lie in the range $4900 < v_p < 5800$ m/s. This is consistent with the findings from borehole logs (Shakas, 2019) that the host rock is moderately disturbed. The velocity variations can be further quantified using the seismic rock quality designation factor (SRQD) introduced

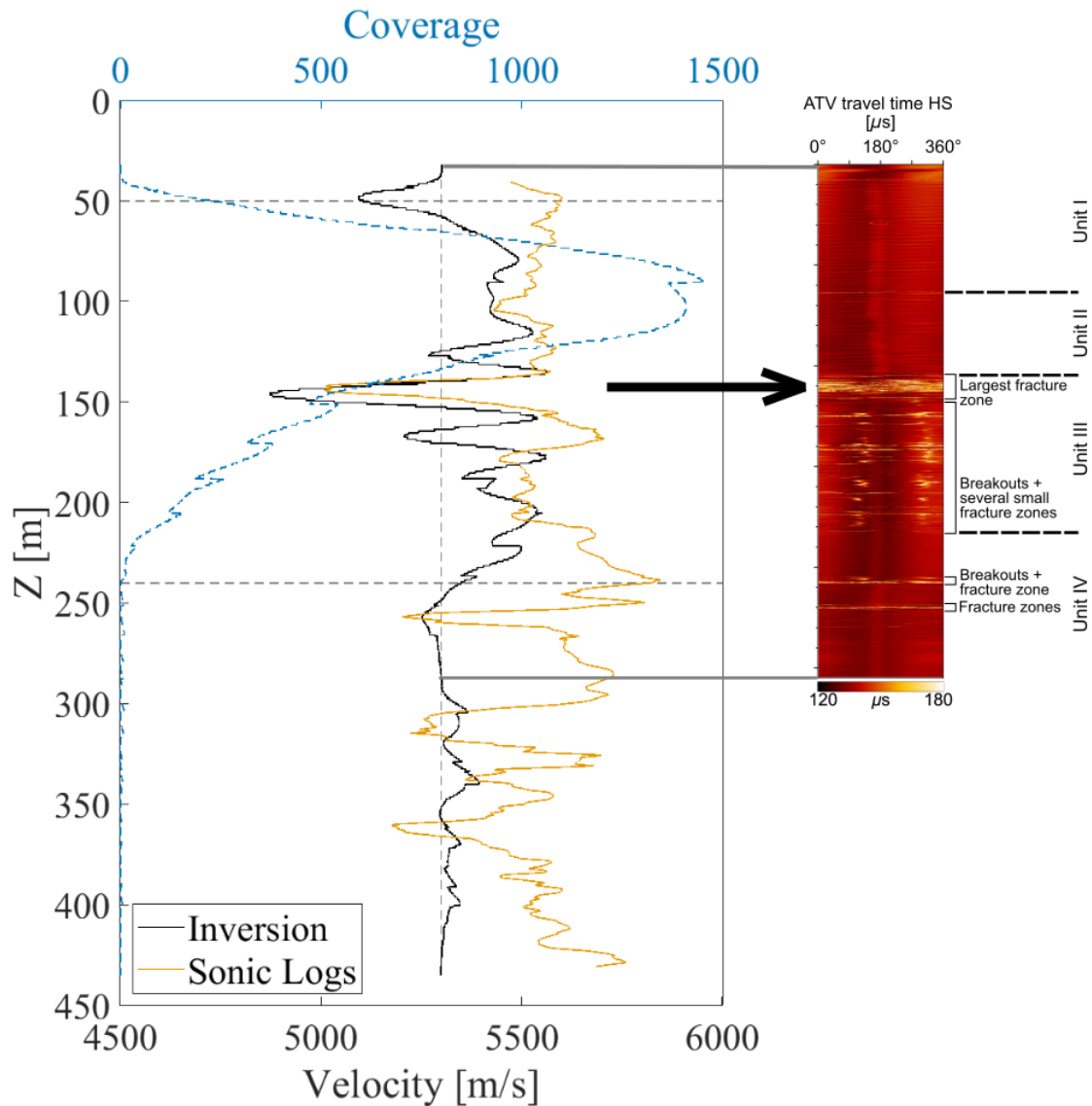


Figure 9. Comparison of the inversion results with geological data. For this purpose, the tomographic velocities (black line) are extracted along the borehole ST1 (in the middle of the volume) and compared to the sonic logs (orange line). The coverage along ST1 is shown in blue. The horizontal gray dashed lines indicate the zone of reasonable good coverage, between 50 m and 250 m depths. We compare the results with ATP logs (on the right) from ST1, which show a fractured zone, that match the low-velocity zone. For the ATP's we adjusted Figure 3 from Bröker et al. (2024) such that the depth is matching the inversion coordinate system used in this paper.



by Deere and Miller (1966):

$$250 \quad SRQD = \left(\frac{v_p}{v_p^{lab}} \right)^2 \times 100. \quad (4)$$

v_p^{lab} is the velocity of the intact rock measured in the laboratory, which is 6123 m/s for the BedrettoLab (David et al., 2020). According to Deere and Deere (1988), the SRQD is a good approximation to the rock quality designation factor (RQD). The SRQD values within our tomographic model lie between 64 and 90, which translates to a rock quality from "fair" to "good/excellent" (Deere and Deere, 1988). This is consistent with geological observations in the geothermal testbed (Ma et al., 2022).

5.6 Limitations of the tomographic velocity model

For an appropriate interpretation of the structures found in the tomographic 3D model, it is necessary to consider its inherent limitation. First of all, the spatial resolution needs to be considered. It is influenced by the ray coverage within the model and the seismic wavelengths. As shown in Figures 7 and 8, the coverage of the fat rays is generally high and homogeneous. Williamson and Worthington (1993) demonstrated that the spatial resolution scales approximately with the width of the Fresnel zone. For a frequency of 2 kHz and an average source-receiver distance of about 50 m, the width of the Fresnel zone is approximately 10 m, which corresponds quite well with minimum feature size in the fat ray tomograms.

Further factors that may limit the reliability of the tomograms include the presence of seismic anisotropy and accuracy of the borehole traces. As already indicated earlier, minor anisotropy effects may exist, but we have chosen to employ an isotropic model. Ignoring significant anisotropy effects during an isotropic inversion would result in layered structures with alternating high and low velocities, thereby mimicking anisotropy. We did not spot a pronounced layering in our tomograms. Similarly, in the presence of significant borehole trace errors, one would expect velocity anomalies towards the bottom of the boreholes, where the formal resolution is worst and anomalies, caused by systematic errors, can develop most easily (Maurer and Green, 1997). Again such effects are not observed in our tomograms. Although we can exclude major artifacts from systematic errors introduced by anisotropy and borehole trace inaccuracies, it cannot be excluded that they may have introduced minor distortions. Therefore, only gross features in the tomograms should be interpreted.

5.7 Comparison of seismic velocities with acoustic emission (AE) events

In 2022 and 2023, several hydraulic stimulation experiments were conducted in the geothermal testbed. The stimulations were performed by injecting water in selected packer intervals of borehole ST1 (see also Section 2). An overview of these experiments in the context of induced seismicity is presented in Obermann et al. (2024). The analysis was performed with DugSeis (Rosskopf et al., 2024b), and more details are provided in Rosskopf et al. (2024a). The stimulations were subdivided in several phases. We restrict ourselves to events recorded during Phase I. In this phase, eight intervals in the range of $121.1 < z < 299.54 \text{ m}$ were stimulated in a consistent manner with similar injection protocols (Bröker et al., 2024; Doonechaly et al., 2024).

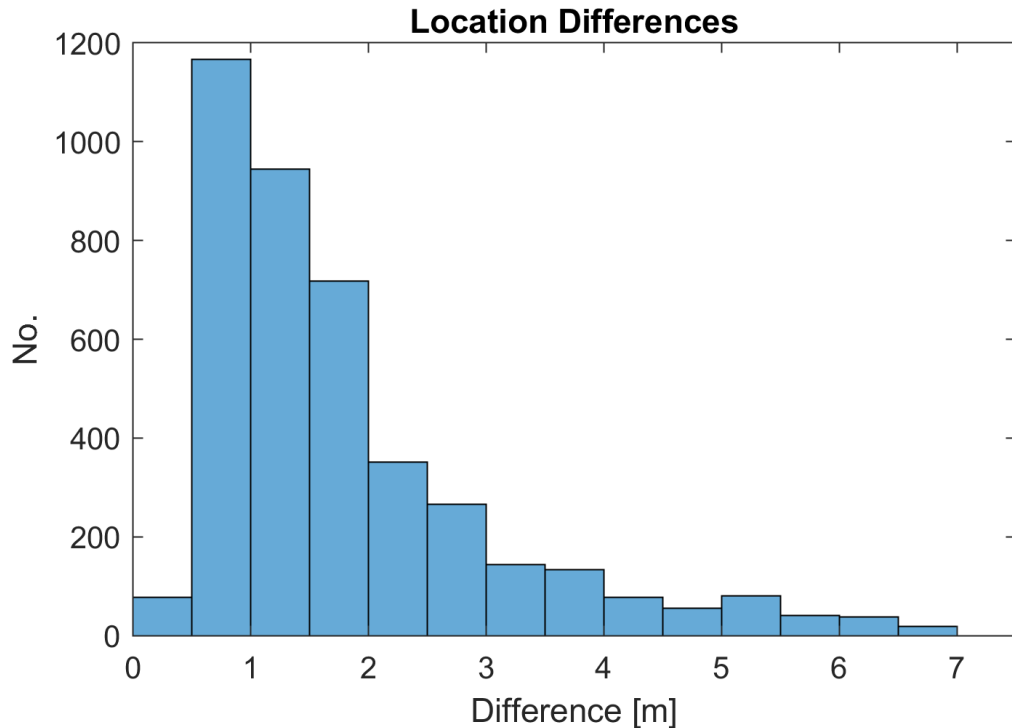
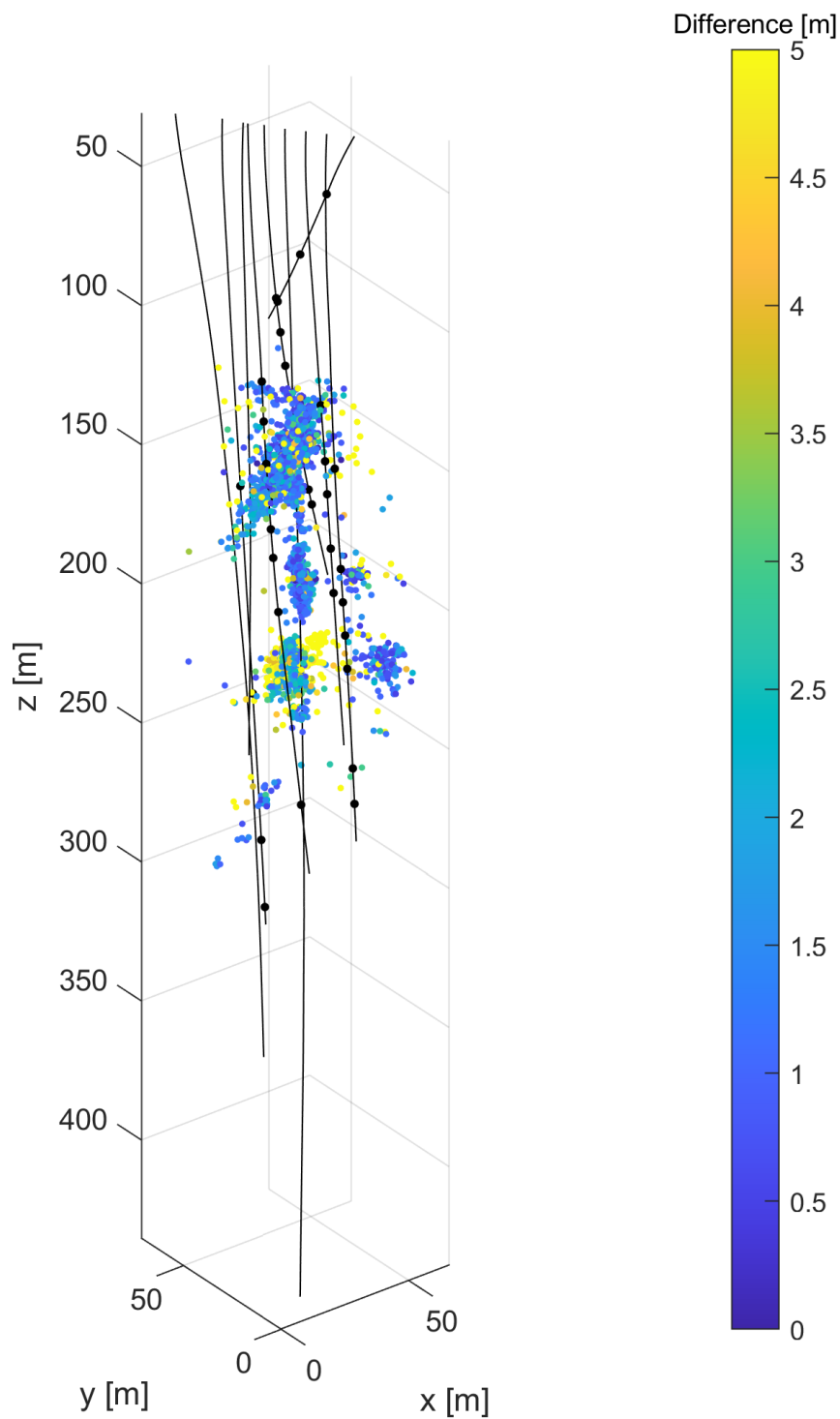


Figure 10. Histogram of the location differences using either a homogeneous or the 3D tomographic model.

For our analyses, we started with the so-called HQ (high quality) events, as described in Obermann et al. (2024). We then restricted our selection to those events lying within the tomographic model. Subsequently, we applied an additional filtering by selecting events that (i) had at least 6 reliable P wave picks (i.e., with corresponding residuals ≤ 0.75 ms), (ii) an RMS misfit of less than 0.5 ms (iii) a determinant of the corresponding Jacobian matrix of more than $1e^{-7}$ (essentially the D-criterion used 285 by Kijko (1977) . This selection procedure left 4283 events that were considered for further analysis. The selected events were finally relocated using the 3D tomographic model, presented in this study, and a grid-search location algorithm similar to the methodology described in Moser et al. (1992). For that purpose, we upsampled the velocity model to a grid spacing of 0.5 m. In Figures 10 and 11, the effects of the 3D model on the locations are illustrated. We located the events with the 3D tomographic model and a homogeneous model with the average velocity (5340 m/s) using the same grid search algorithm, and analysed the 290 differences. The histogram in Figure 10 demonstrates that most differences are rather small (mean difference: 2.2 m, median difference: 1.4 m), and the spatial distribution of the differences in Figure 11 indicate that the effects of the 3D model tend to be slightly more pronounced at $z > 220$ m. It is also noteworthy that there is no systematic shift between the two location algorithms. From these observations we conclude that the effect of the 3D model on the hypocentral locations is quite minor, which is in agreement with the investigations of Rosskopf et al. (2024a).





However, it is interesting to consider the spatial correlation between the seismic activity and the seismic velocities. For that purpose, we subdivide the velocity model into **low- intermediate** and high-velocity regions, and compare them with the predominant locations of the seismicity. Low and high velocity regions are defined as zones, in which the velocities are either lower or higher than one standard deviation ($\approx 150 \text{ m/s}$) from the mean velocity ($\approx 5340 \text{ m/s}$) of the resolved areas within 300 the 3D tomogram.

For the analysis, we consider horizontal slices through the region of interest, as well as a vertical slice approx. perpendicular to the **MFZ**. For each slice, we superimpose the seismic events that have occurred on or near ($\pm 2.5 \text{ m}$) **the slices**. The results are shown in Figures 12 and 13, and movies, showing all horizontal and vertical slices, are provided in the digital appendix.

We observe a conspicuous correlation between the seismicity and the velocity pattern. The seismic events seem to "avoid" 305 the high velocity (blue) regions, and they occur rarely within the regions of very low velocities (dark red). The majority of the events can be found in the regions of intermediate and slightly decreased velocities (grey and light red), and some of the slices show a **remarkable** event clustering along the boundaries between intermediate and high velocities (e.g., Figure 13b). A deviation of this correlation is found in areas near the injection borehole ST1 (marked red in Figure 12). Here, the AE activity 310 is tightly coupled with the injection process itself.

310 A rather qualitative interpretation of these observations could be as follows. High velocity areas represent intact host rock, and the injection pressures (up to approximately 18 MPa) were apparently insufficient to break up these areas. Very low velocities may represent considerably fractured zones, where it is no longer possible to accumulate sufficient stress levels, such that significant seismic activity can occur. In intermediate velocity regions, pre-existing fractures may exist, but the rock strength is still high enough, such that stress accumulation and subsequent break-up can occur. It should be noted that the crosshole 315 measurements were performed prior to the injections, and represent thus the state prior to the injection experiments. However, this is of minor importance, since we expect only very minor velocity changes caused by the injections. Initial analyses of repeated active seismic measurements during the stimulation experiments indicated that the expected velocity changes are well below 1 %. For a more detailed interpretation, we consider the relationship between seismic velocities and mechanical 320 stiffness, which are linked through elasticity and continuum mechanics (e.g., Mavko et al. (2009)). Microcracking and pore fluids significantly influence these velocities (e.g. Paterson and Wong (2005)). Damage, characterized by microfracturing, is a key indicator of brittle deformation in geological settings, extensively documented in natural fault zones (e.g. Faulkner et al. (2010), and references therein). Laboratory rock failure tests demonstrate that increased microcracking reduces wave speeds 325 and stiffness (e.g. Stanchits et al. (2011)).

The variation in stiffness, inferred from seismic velocities, likely produces strain gradients between the slower, damaged 325 material and the stiffer, intact rock matrix during fluid injection tests. The strain gradient reflects, how the deformation will vary throughout the body, resulting in stress concentrations over the velocity gradient. This mechanism has explained the patterns of AEs in the Rotondo granite in laboratory test (Salazar Vásquez et al., 2024) and has also been proposed to explain rock bursts around the EDZ in mining environments (Barton, 2006) (Chap. 7.2).

A complementary mechanism for the AEs produced in the medium and lower velocity zones is that permeability increases 330 with the presence of connected microcracks and damage. The lower and medium velocity regions present preexisting higher



permeability zones. During fluid injection, the pore fluid pressure will migrate preferentially into these regions. If these regions have preexisting structures that are preferentially oriented and close to failure, only small fluid pressure perturbation would be needed to induce failure (Townend and Zoback, 2000).

It is **remarkable** that similar observations were made in the laboratory (i.e., centimeter scale, (Salazar Vásquez et al., 2024)) 335 and within our geothermal testbed (decameter scale), and it is even more interesting to note that similar observations can also be made at larger scale. Local earthquake tomography investigations in the **Hengill geothermal field** (kilometer scale) (Obermann et al., 2022) also show a clustering of the seismic events in zones of intermediate velocities. Therefore, it seems that the underlying mechanisms are pretty much scale independent.

6 Conclusions

340 The experimental setup of the geothermal testbed in the BedrettoLab offered unique opportunities for 3D tomographic studies. The literature on such investigations on that scale is very sparse - in fact, we could not find a comparable study in the literature. Our finding could thus be a motivation for other experiments in similar environments.
We can clearly show that in comparison with traditional thin ray methods, fat ray tomography does not only better mimic the physics of band-limited seismic data, but it also results in an improved coverage. It is also worthwhile mentioning that fat 345 ray tomography **is less dependent on the model parametrization of the forward and inversion grids (compared with thin rays)**, because the sensitivity kernels are governed primarily by the (prescribed) dominant wavelength of the seismic data.
There are two main findings from the analysis of the 3D velocity model. First, we could characterize one of the major fault zones. Its signature in the tomographic image is not a narrow and well confined zone of decreased velocities, as one would expect. Instead, it is distinguished by a relatively large volume of generally decreased velocities with considerable heterogeneities. Secondly, we found a spatial correlation between passive seismic events, generated by hydraulic stimulations, and the tomographically derived velocity structures. The passive seismic events occur between high and very low velocity zones. 350 Based on similar results from a small-scale laboratory study, we attribute this observation to the existence of stress gradients in the regions of intermediate velocities.

Data availability. The input data for the inversion is published by Maurer and Schwarz (2025): <https://doi.org/10.3929/ethz-b-000725491>.
355 Seismicity catalogs of the VALTER project have been published by Rosskopf et al. (2024a)

Video supplement. Video supplements for the 3D velocity model are published by Maurer and Schwarz (2025) <https://doi.org/10.3929/ethz-b-000725491>

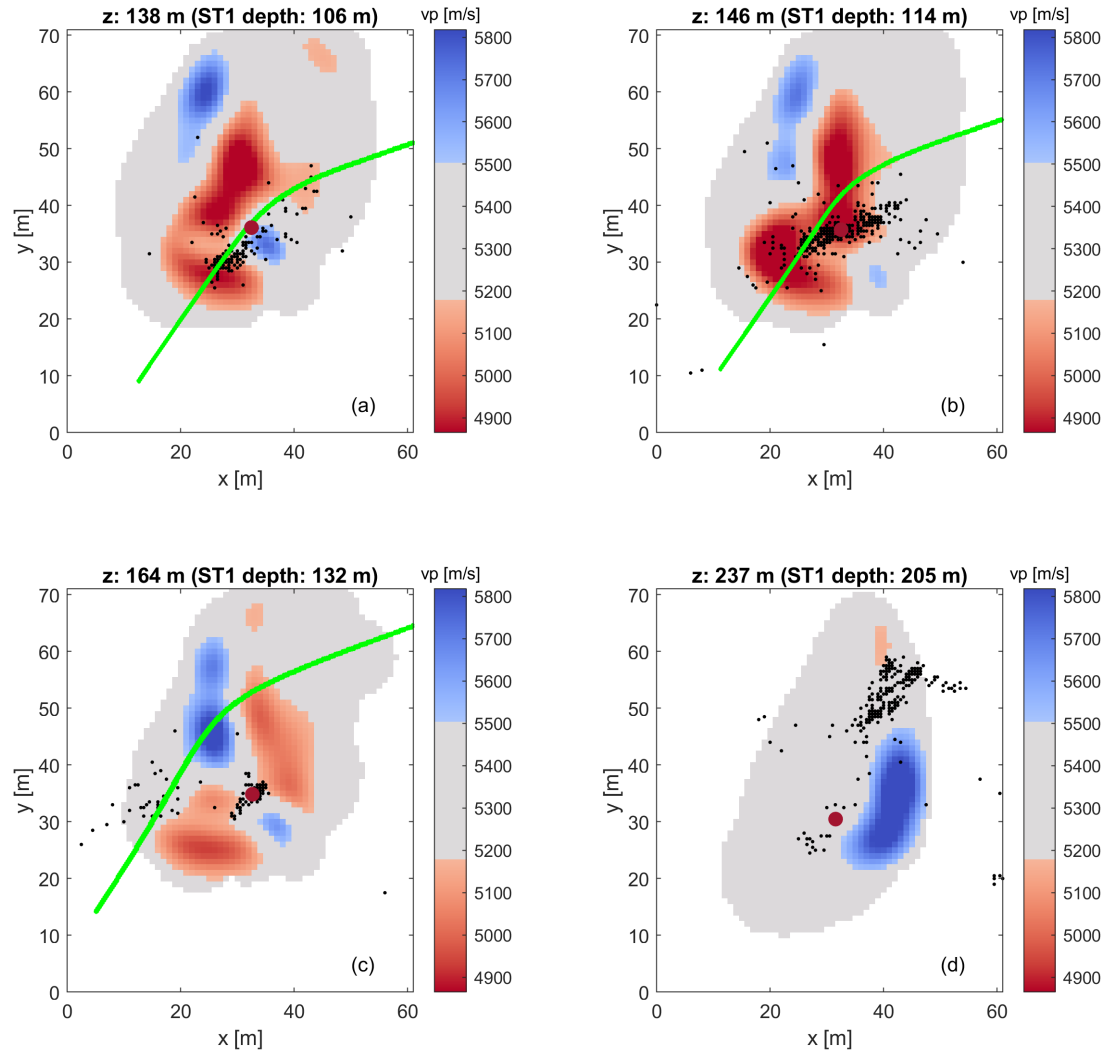


Figure 12. Horizontal slices through the tomographic model. Low and high velocities are shown in red and blue, and intermediate velocity areas are shown gray. The seismicity located ± 2.5 m distance from the slices is superimposed by black dots. The intersection of the MFZ is shown in light green.

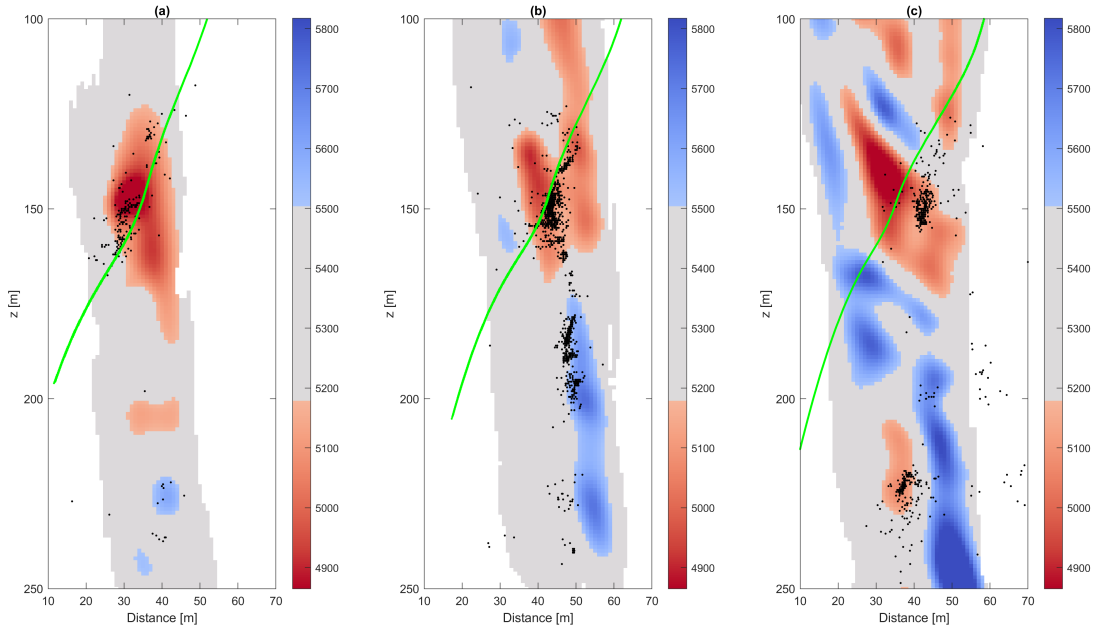


Figure 13. Vertical slices perpendicular to the MFZ through the tomographic model. The slices are located near the trace of the injection borehole ST1. Low and high velocities are shown in red and blue, and intermediate velocity areas are shown gray. The seismicity located ± 2.5 m distance from the slices is superimposed by black dots. The intersection of the MFZ is shown in light green.

Author contributions. MLS performed the data analysis, the Inversion and wrote the paper. HM supervised MLS, performed the earthquake relocation and wrote/edited the paper. AO and AS organized the data acquisition, performed preliminary tests and edited the paper. PAS 360 edited the paper. HM, SW and DG supervised the project.

Competing interests. The authors declare that they have no conflict of interest.

Acknowledgements. In the "Bedretto Underground Laboratory for Geosciences and Geoenergies", ETH Zurich studies in close collaboration with national and international partners techniques and procedures for a safe, efficient, and sustainable use of geothermal heat and questions related to earthquake physics. The BedrettoLab is financed by the Werner Siemens Foundation, ETH Zürich and the Swiss National Science 365 Foundation. Miriam Schwarz is founded by the SNF Multi PhD (200021_192151) project. The research in this publication has received additional funding by the project VALTER (Validierung von Technologien zur Reservoir Entwicklung) (SI/501496-01). The BedrettoLab would like to thank Matterhorn Gotthard Bahn for providing access to the tunnel. We would like to thank Kai Bröker for his feedback on



section 2, particularly regarding fracture mapping in the BedrettoLab. We thank the BedrettoLab Operation Team, led by Marian Hertrich, for their excellent support, which was essential for this project. This paper is BULGG publication BPN_029



370 **References**

Amann, F., Gischig, V., Evans, K., Doetsch, J., Jalali, R., Valley, B., Krietsch, H., Dutler, N., Villiger, L., Brixel, B., Klepikova, M., Kittilä, A., Madonna, C., Wiemer, S., Saar, M. O., Loew, S., Driesner, T., Maurer, H., and Giardini, D.: The seismo-hydromechanical behavior during deep geothermal reservoir stimulations: Open questions tackled in a decameter-scale in situ stimulation experiment, <https://doi.org/10.5194/se-9-115-2018>, 2018.

375 Barton, N.: Rock Quality, Seismic Velocity, Attenuation and Anisotropy, CRC Press, ISBN 9781134160136, <https://doi.org/10.1201/9780203964453>, 2006.

Behnen, K., Hertrich, M., Maurer, H., Shakas, A., Bröker, K., Epiney, C., Blanch Jover, M., and Giardini, D.: Investigation of Seismic Anisotropy in the Undisturbed Rotondo Granite, <https://doi.org/10.5194/egusphere-2024-1919>, 2024.

Block, L. V., Cheng, C. H., Fehler, M. C., and Phillips, W. S.: Seismic imaging using microearthquakes induced by hydraulic fracturing, 380 Geophysics, 59, 102–112, <https://doi.org/10.1190/geo1992-0156>, 1994.

Bröker, K. and Ma, X.: Estimating the Least Principal Stress in a Granitic Rock Mass: Systematic Mini-Frac Tests and Elaborated Pressure Transient Analysis, Rock Mechanics and Rock Engineering, 55, 1931–1954, <https://doi.org/10.1007/s00603-021-02743-1>, 2022.

385 Bröker, K., Ma, X., Gholizadeh Doonechaly, N., Rosskopf, M., Obermann, A., Rinaldi, A. P., Hertrich, M., Serbeto, F., Maurer, H., Wiemer, S., and Giardini, D.: Hydromechanical characterization of a fractured crystalline rock volume during multi-stage hydraulic stimulations at the BedrettoLab, Geothermics, 124, <https://doi.org/10.1016/j.geothermics.2024.103126>, 2024.

Červený, V. and Soares, J. E. P.: Fresnel volume ray tracing, GEOPHYSICS, 57, 902–915, <https://doi.org/10.1190/1.1443303>, 1992.

Charléty, J., Cuenot, N., Dorbath, C., and Dorbath, L.: Tomographic study of the seismic velocity at the Soultz-sous-Forêts EGS/HDR site, Geothermics, 35, 532–543, <https://doi.org/10.1016/j.geothermics.2006.10.002>, 2006.

390 David, C., Nejati, M., and Geremia, D.: On petrophysical and geomechanical properties of Bedretto Granite, Tech. rep., <https://doi.org/10.5194/egusphere-2025-1094>, 2020.

Deere, D. and Deere, D.: The Rock Quality Designation (RQD) in Practice, Rock Classification Systems for Engineering Purposes, ASTM STP 984, pp. 91–101, 1988.

Deere, D. and Miller, R.: Classification and index properties of intact rock, New Mexico, 1966.

395 Doonechaly, N. G., Bröker, K., Hertrich, M., Rosskopf, M., Obermann, A., Durand, V., Serbeto, F., Shakas, A., Ma, X., Rinaldi, A. P., Repollés, V. C., Villiger, L., Meier, M.-A., Gischig, V., Plenkers, K., Maurer, H., Wiemer, S., and Giardini, D.: Insights from Subsurface Monitoring for Engineering of the Stimulation Pattern in Fractured Reservoirs, <https://doi.org/10.21203/rs.3.rs-4859925/v1>, 2024.

Edwards, B., Kraft, T., Cauzzi, C., Kästli, P., and Wiemer, S.: Seismic monitoring and analysis of deep geothermal projects in St Gallen and Basel, Switzerland, Geophysical Journal International, 201, 1022–1039, <https://doi.org/10.1093/gji/ggv059>, 2015.

400 Ellsworth, W. L., Giardini, D., Townend, J., Ge, S., and Shimamoto, T.: Triggering of the Pohang, Korea, Earthquake (Mw 5.5) by enhanced geothermal system stimulation, <https://doi.org/10.1785/0220190102>, 2019.

Escallón, D., Shakas, A., and Maurer, H.: Modelling and inferring fracture curvature from borehole GPR data: A case study from the Bedretto Laboratory, Switzerland, Near Surface Geophysics, 22, 235–254, <https://doi.org/10.1002/nsg.12286>, 2024.

Faulkner, D. R., Jackson, C. A., Lunn, R. J., Schlische, R. W., Shipton, Z. K., Wibberley, C. A., and Withjack, M. O.: A review of recent developments concerning the structure, mechanics and fluid flow properties of fault zones, <https://doi.org/10.1016/j.jsg.2010.06.009>, 2010.

405 Gischig, V. S., Giardini, D., Amann, F., Hertrich, M., Krietsch, H., Loew, S., Maurer, H., Villiger, L., Wiemer, S., Bethmann, F., Brixel, B., Doetsch, J., Doonechaly, N. G., Driesner, T., Dutler, N., Evans, K. F., Jalali, M., Jordan, D., Kittilä, A., Ma, X., Meier, P., Nejati,



M., Obermann, A., Plenkers, K., Saar, M. O., Shakas, A., and Valley, B.: Hydraulic stimulation and fluid circulation experiments in underground laboratories: Stepping up the scale towards engineered geothermal systems, *Geomechanics for Energy and the Environment*, 24, <https://doi.org/10.1016/j.gete.2019.100175>, 2020.

410 Heidbach, O., Rajabi, M., Cui, X., Fuchs, K., Müller, B., Reinecker, J., Reiter, K., Tingay, M., Wenzel, F., Xie, F., Ziegler, M. O., Zoback, M. L., and Zoback, M.: The World Stress Map database release 2016: Crustal stress pattern across scales, <https://doi.org/10.1016/j.tecto.2018.07.007>, 2018.

Heincke, B., Maurer, H., Green, A. G., Willenberg, H., Spillmann, T., and Burlini, L.: Characterizing an unstable mountain slope using shallow 2D and 3D seismic tomography, *Geophysics*, 71, <https://doi.org/10.1190/1.2338823>, 2006.

415 Hirschberg, S., Wiemer, S., and Burgherr, P. e.: Energy from the earth Deep geothermal as a resource for the future?, TA-SWISS, 2015, <https://doi.org/10.3929/ethz-a-010277690>, 2015.

Holliger, K., Musil, M., and Maurer, H. R.: Ray-based amplitude tomography for crosshole georadar data: a numerical assessment, *Tech. rep.*, www.elsevier.comrlocaterjappgeo, 2001.

Husen, S. and Kissling, E.: Local earthquake tomography between rays and waves: fat ray tomography, *Tech. rep.*, ISBN 00319201/01, 2001.

420 Jordan, D.: Geological Characterization of the Bedretto Underground Laboratory for Geoenergies, ETH Zurich Research Collection, <https://doi.org/10.3929/ethz-b-000379305>, 2019.

Jordi, C., Schmelzbach, C., and Greenhalgh, S.: Frequency-dependent traveltimes tomography using fat rays: application to near-surface seismic imaging, *Journal of Applied Geophysics*, 131, 202–213, <https://doi.org/10.1016/j.jappgeo.2016.06.002>, 2016.

Kijko, A.: An Algorithm for the Optimum Distribution of a Regional Seismic Network-I, *Pageoph*, 115, 999–1009, 1977.

425 Kneafsey, T., Dobson, P., Blankenship, D., Schwering, P., White, M., Morris, J. P., Huang, L., Johnson, T., Burghardt, J., Mattson, E., Neupane, G., Strickland, C., Knox, H., Vermuel, V., Ajo-Franklin, J., Fu, P., Roggenthen, W., Doe, T., Schoenball, M., Hopp, C., Tribaldos, V. R., Ingraham, M., Guglielmi, Y., Ulrich, C., Wood, T., Frash, L., Pyatina, T., Vandine, G., Smith, M., Horne, R., McClure, M., Singh, A., Weers, J., and Robertson, M.: The EGS Collab project: Outcomes and lessons learned from hydraulic fracture stimulations in crystalline rock at 1.25 and 1.5 km depth, *Geothermics*, 126, <https://doi.org/10.1016/j.geothermics.2024.103178>, 2025.

430 Labhart T: Erläuterungen Zum Geologischen Atlas Des Schweiz 1:25000, Val Bedretto, 2005.

Lanz, E., Maurer, H., and Green, A. G.: Refraction tomography over a buried waste disposal site, *Geophysics*, 63, 1414–1433, <https://doi.org/10.1190/1.1444443>, 1998.

Li, B., Ding, L., Hu, D., and Zheng, S.: Backtracking Algorithm-based Disassembly Sequence Planning, in: *Procedia CIRP*, vol. 69, pp. 932–937, Elsevier B.V., ISSN 22128271, <https://doi.org/10.1016/j.procir.2017.12.007>, 2018.

435 Lützenkirchen, V. and Loew, S.: Late Alpine brittle faulting in the Rotondo granite (Switzerland): Deformation mechanisms and fault evolution, *Swiss Journal of Geosciences*, 104, 31–54, <https://doi.org/10.1007/s00015-010-0050-0>, 2011.

Ma, X., Hertrich, M., Amann, F., Bröker, K., Doonechaly, N. G., Gischig, V., Hochreutener, R., Kästli, P., Krietsch, H., Marti, M., Nägeli, B., Nejati, M., Obermann, A., Plenkers, K., Rinaldi, A. P., Shakas, A., Villiger, L., Wenning, Q., Zappone, A., Bethmann, F., Castilla, R., Seberto, F., Meier, P., Driesner, T., Loew, S., Maurer, H., Saar, M. O., Wiemer, S., and Giardini, D.: Multi-disciplinary characterizations 440 of the BedrettoLab-A new underground geoscience research facility, *Solid Earth*, 13, 301–322, <https://doi.org/10.5194/se-13-301-2022>, 2022.

Maurer, H. and Green, A. G.: Potential coordinate mislocations in crosshole tomography: Results from the Grimsel test site, Switzerland, *Tech. Rep.* 6, <http://pubs.geoscienceworld.org/geophysics/article-pdf/62/6/1696/3172949/1696.pdf>, 1997.



445 Maurer, H. and Schwarz, M. L.: Data collection to: New insights on the fault structure of a geothermal testbed and the associated seismicity based on active seismic tomography, <https://doi.org/10.3929/ETHZ-B-000725491>, 2025.

Maurer, H., Holliger, K., and Boerner, D. E.: Stochastic regularization: Smoothness or similarity?, *Geophysical Research Letters*, 25, 2889–2892, <https://doi.org/10.1029/98GL02183>, 1998.

Mavko, G., Mukerji, T., and Dvorkin, J.: *The Rock Physics Handbook*, Cambridge University Press, 2nd edition edn., ISBN 9780521861366, <https://doi.org/10.1017/CBO9780511626753>, 2009.

450 Meier, M.: Geological characterisation of an underground research facility in the Bedretto tunnel, ETH Zurich Research Collection, <https://doi.org/10.3929/ethz-b-000334001>, 2017.

Menke, W.: *Geophysical Data Analysis: Discrete Inverse Theory*, Elsevier, ISBN 9780124909205, <https://doi.org/10.1016/B978-0-12-490920-5.X5001-7>, 1984.

Moser, T. J., Van Eck, T., and Nolet, G.: Hypocenter determination in strongly heterogeneous Earth models using the shortest path method, <https://doi.org/10.1029/91JB03176>, 1992.

455 Nakagome, O., Uchida, T., and Horikoshi, T.: Seismic reflection and VSP in the kakkonda geothermal field, japan: fractured reservoir characterization, *Geothermics*, 27, 535–552, [https://doi.org/10.1016/S0375-6505\(98\)00032-7](https://doi.org/10.1016/S0375-6505(98)00032-7), 1998.

Nakata, N., Vasco, D. W., Shi, P., Bai, T., Lanza, F., Dyer, B., Chen, C., Park, S.-E., and Qiu, H.: *Elastic Characterization at Utah FORGE: P-wave Tomography and VSP Subsurface Imaging*, Tech. rep., 2023.

460 Nolet, G.: *Seismic Tomography*, Springer Netherlands, Dordrecht, ISBN 978-90-277-2583-7, <https://doi.org/10.1007/978-94-009-3899-1>, 1987.

Obermann, A. and Hillers, G.: Seismic time-lapse interferometry across scales, in: *Advances in Geophysics*, vol. 60, pp. 65–143, Academic Press Inc., ISBN 9780128175484, <https://doi.org/10.1016/bs.agph.2019.06.001>, 2019.

Obermann, A., Wu, S. M., Ágústsdóttir, T., Duran, A., Diehl, T., Sánchez-Pastor, P., Kristjansdóttir, S., Hjörleifsdóttir, V., Wiemer, S., and 465 Hersir, G. P.: Seismicity and 3-D body-wave velocity models across the Hengill geothermal area, SW Iceland, *Frontiers in Earth Science*, 10, <https://doi.org/10.3389/feart.2022.969836>, 2022.

Obermann, A., Rosskopf, M., Plenkers, K., Broeker, K., Rinaldi, A., Doonechaly, N., Gischig, V., Zappone, A., Amann, F., Cocco, M., Hertrich, M., Jalali, M., Junker, J., Kästli, P., Ma, X., Maurer, H., Meier, M.-A., Schwarz, M., Selvadurai, P., and Giardini, D.: Seismic response of hectometer-scale fracture systems to hydraulic stimulation in the Bedretto Underground laboratory, Switzerland, *Journal of 470 Geophysical Research: Solid Earth*, <https://doi.org/10.1029/2024JB029836>, 2024.

Olasolo, P., Juárez, M. C., Morales, M. P., Damico, S., and Liarte, I. A.: Enhanced geothermal systems (EGS): A review, <https://doi.org/10.1016/j.rser.2015.11.031>, 2016.

Paige, C. C. and Saunders, M. A.: LSQR: An Algorithm for Sparse Linear Equations and Sparse Least Squares, pp. 43–71, 1982.

Paterson, M. S. and Wong, T.-f.: *Experimental Rock Deformation – The Brittle Field*, Springer-Verlag Berlin Heidelberg 2005, second edition 475 edn., ISBN 978-3-540-24023-5, 2005.

Place, J., Sausse, J., Marthelot, J. M., Diraison, M., Géraud, Y., and Naville, C.: 3-D mapping of permeable structures affecting a deep granite basement using isotropic 3C VSP data, *Geophysical Journal International*, 186, 245–263, <https://doi.org/10.1111/j.1365-246X.2011.05012.x>, 2011.

Plenkers, K., Manthei, G., and Kwiatek, G.: *Underground In-situ Acoustic Emission in Study of Rock Stability and Earthquake Physics*, in: 480 *Springer Tracts in Civil Engineering*, pp. 403–476, Springer Science and Business Media Deutschland GmbH, https://doi.org/10.1007/978-3-030-67936-1_16, 2022.



Podvin, P. and Lecomte, I.: Finite difference computation of traveltimes in very contrasted velocity models: a massively parallel approach and its associated tools, Tech. rep., <https://academic.oup.com/gji/article/105/1/271/671376>, 1991.

Pratt, R. G. and Worthington, M. H.: The application of diffraction tomography to cross-hole seismic data, *Geophysics*, 53, 1284–1294, 485 <https://doi.org/10.1190/1.1442406>, 1988.

Roszkopf, M., Durand, V., Plenkers, K., Villiger, L., Giardini, D., and Obermann, A.: Accuracy of picoseismic catalogs in hectometer-scale in-situ experiments, <https://doi.org/10.22541/essoar.172736342.25689581/v1>, 2024a.

Roszkopf, M., Durand, V., Villiger, L., and Doetsch, J.: DUGseis: A Python package for real-time and post-processing of picoseismicity, <https://doi.org/10.21105/joss.06768>, 2024b.

490 Salazar Vásquez, A. F., Selvadurai, P. A., Bianchi, P., Madonna, C., Germanovich, L. N., Puzrin, A. M., Wiemer, S., Giardini, D., and Rabaiotti, C.: Aseismic strain localization prior to failure and associated seismicity in crystalline rock, *Scientific Reports*, 14, <https://doi.org/10.1038/s41598-024-75942-9>, 2024.

Sergeev, S. A., Meier, M., and Steiger, R. H.: EPSL Improving the resolution of single-grain U/Pb dating by use of zircon extracted from feldspar: Application to the Variscan magmatic cycle in the central Alps, Tech. rep., 1995.

495 Shakas, A.: Borehole Logging Data from Characterization Boreholes in Bedretto Underground Lab for Geoenergies, 2019.

Stanchits, S., Mayr, S., Shapiro, S., and Dresen, G.: Fracturing of porous rock induced by fluid injection, *Tectonophysics*, 503, 129–145, <https://doi.org/10.1016/j.tecto.2010.09.022>, 2011.

Townend, J. and Zoback, M. D.: How faulting keeps the crust strong, *GEOLOGY*, 28, 399–402, 2000.

Williamson, P. R. and Worthington, M. H.: Resolution limits in ray tomography due to wave behavior: numerical experiments, *Geophysics*, 500 58, 727–735, <https://doi.org/10.1190/1.1443457>, 1993.

Woodward, M. J.: Wave-equation tomography, *Geophysics*, 57, 15–26, <https://doi.org/10.1190/1.1443179>, 1992.

Zelt, C. A. and Barton, P. J.: Three-dimensional seismic refraction tomography: A comparison of two methods applied to data from the Faeroe Basin, <https://doi.org/10.1029/97jb03536>, 1998.